https://doi.org/10.1038/s41557-022-00892-6



Quantum-classical simulations of rhodopsin reveal excited-state population splitting and its effects on quantum efficiency

Xuchun Yang 1, Madushanka Manathunga 1, Samer Gozem 2, Jérémie Léonard, Tadeusz Andruniów 64 and Massimo Olivucci 1,5,6 🖂

The activation of rhodopsin, the light-sensitive G-protein-coupled receptor responsible for dim-light vision in vertebrates, is driven by an ultrafast excited-state double-bond isomerization with a quantum efficiency of almost 70%. The origin of such light sensitivity is not understood and a key question is whether in-phase nuclear motion controls the quantum efficiency value. In this study we used hundreds of quantum-classical trajectories to show that, 15 fs after light absorption, a degeneracy between the reactive excited state and a neighbouring state causes the splitting of the rhodopsin population into subpopulations. These subpopulations propagate with different velocities and lead to distinct contributions to the quantum efficiency. We also show here that such splitting is modulated by protein electrostatics, thus linking amino acid sequence variations to quantum efficiency modulation. Finally, we discuss how such a linkage that in principle could be exploited to achieve higher quantum efficiencies would simultaneously increase the receptor thermal noise leading to a trade-off that may have played a role in rhodopsin evolution.

hodopsin (Rh) features an 11-cis-retinal protonated Schiff base (rPSB11) chromophore covalently bound to a protein (opsin) cavity formed by seven α -helices¹. As illustrated in Fig. 1a, absorption of a photon induces a sub-picosecond isomerization of rPSB11 to its all-trans stereoisomer (rPSBAT), which initiates the receptor photocycle and, ultimately, visual transduction¹⁻⁴. The Rh photoisomerization has a low thermal noise⁵ that, when combined with its 0.67 quantum efficiency ($\Phi_{cis-trans}$)⁶, results in an extremely high light sensitivity. The photoisomerization has also been reported to display a coherent (that is, phased) nuclear motion of the molecular population along the reaction coordinate⁷⁻¹⁰. Such phased motion is attributed to the dynamics induced by the potential energy surface (PES) of the reactive excited state. In other words, the nuclear forces created by the PES slope impose specific phase relationships between the modes describing the rPSB11 transfer from the first singlet excited state (S_1) to the ground state (S_0) .

Three rPSB11 modes are implicated in the S₁-to-S₀ transfer (Fig. 1b)^{11,12}. These are the C11=C12 counterclockwise twist (α), the hydrogen out-of-plane deformation of the HC11=C12H hydrogen atoms (β) and the skeletal bond length alternation (BLA) stretching of the conjugated backbone. In Fig. 1c we also conveniently define the dihedral angles δ_{op} , representing the hydrogen out-of-plane deformation relative to the carbon skeleton, and τ , representing the orbital overlap across the isomerizing bond. As shown in Fig. 1c, the S₁-to-S₀ transfer is described in terms of the progression along a multimode coordinate connecting the S₁ vertical excitation region of the PES to a decay region in the vicinity of the S_1/S_0 intersection space $(IS_{S1/S_0})^{12}$.

Past results¹³ have shown that the relationship between the phases of specific modes determines whether rPSB11 would proceed towards rPSBAT and form the bathorhodopsin (bathoRh) photoproduct or relax back to its starting configuration¹. More specifically, at the single-molecule level, the relationship between the phases of the velocities of lpha and $\delta_{ ext{op}}$ at decay determines whether the isomerization is successful or unsuccessful 11,13,14 . The change in δ_{op} appears to be critical. Its physical meaning implies that, to generate bathoRh, the H11/H12 hydrogen rotation described by angle β (Fig. 1b) shall decrease faster than the decrease in the skeletal isomerization described by α . Only when this condition, yielding a positive δ_{op} change, is satisfied, the orbital overlap (proportional to τ) changes direction, thus allowing for the formation of a trans C11=C12 double bond (see ref. 13 for a more detailed explanation). Thus, as illustrated in Fig. 1d, when the C10/C13 carbon and H11/H12 hydrogen rotations are in-phase, the τ velocity is negative and the decay to S_0 results in a product-like overlap leading to rPSBAT formation. As $\tau = \alpha - \delta_{op}/2$ and α mainly change in the negative counterclockwise direction $(d\alpha/dt < 0)$, a successful isomerization is equivalent to a positive δ_{op} velocity $(d\delta_{op}/dt > 0)$ at decay. The existence of a link between the phases of the α and $\delta_{\rm op}$ velocities and the light sensitivity of Rh has been experimentally demonstrated by showing that deuterium substitutions at H11 and/or H12 modulate $\Phi_{cis-trans}$ (ref. ¹³).

In principle, a population displaying phased nuclear motion along BLA, α and δ_{op} would be able to exploit the mechanism reviewed above to maximize $\Phi_{cis-trans}$. As illustrated in Fig. 1e, this limit would be reached when the largest possible population fraction decays with $d\delta_{op}/dt > 0$. To find out how closely Rh follows such an ideal case, we have employed a hybrid multiconfigurational 15-17 quantum mechanical/molecular mechanics (QM/MM) model of Rh5,18 to study the S1 dynamics of an initially room-temperature S₀ population using 200 quantum-classical trajectories. The results show that the nuclear

Department of Chemistry, Bowling Green State University, Bowling Green, OH, USA. Department of Chemistry, Georgia State University, Atlanta, GA, USA. 3Institut de Physique et Chimie des Matériaux de Strasbourg, Université de Strasbourg, CNRS, Strasbourg, France. 4Department of Chemistry, Wroclaw University of Science and Technology, Wroclaw, Poland. Dipartimento di Biotecnologie, Chimica e Farmacia, Università di Siena, Siena, Italy. Institute for Advanced Studies, University of Strasbourg, Strasbourg, France.

□e-mail: molivuc@bgsu.edu

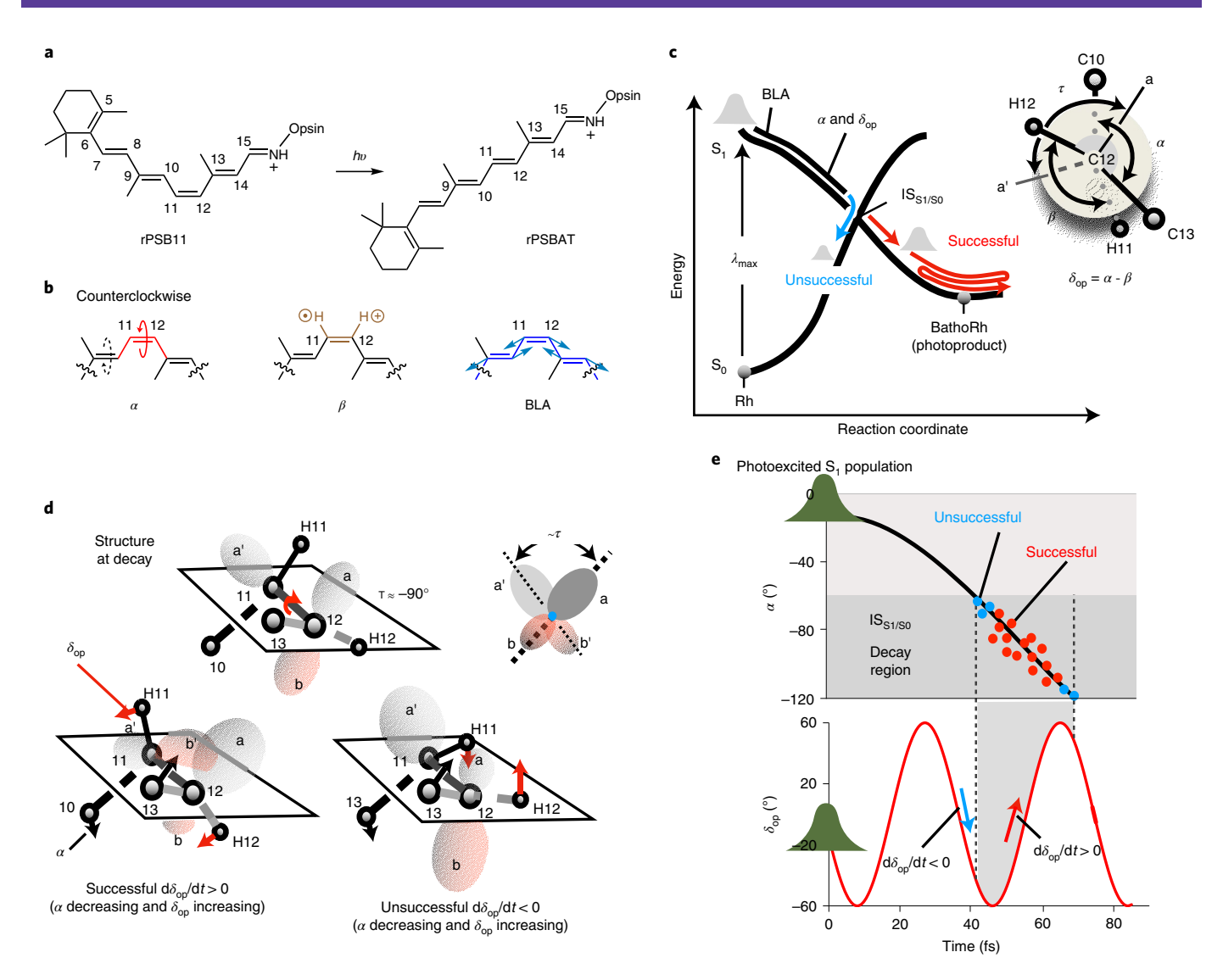


Fig. 1 | Theory of Rh photoisomerization. **a**, Isomerization of rPSB11 to the all-*trans* stereoisomer rPSBAT. **b**, The α (red), β (brown) and BLA (blue) modes contributing to the reaction coordinate. α and β correspond to the C10-C11-C12-C13 and H11-C11-C12-H12 dihedral angles, respectively. BLA is the difference between the average single bond and the average double bond lengths of the rPSB11 backbone connecting C5 and N. The dashed arrow indicates that α is coupled with clockwise C9=C10 twisting to form a bicycle-pedal coordinate 32,33 . The circled cross/dot on β represents the H wagging motion out of/into the carbon framework plane, respectively. **c**, Representation of the evolution of the Rh population on a PES diagram. BLA dominates the early part of the reaction coordinate while a combination of the α and δ_{op} modes (see the Newman projection) drives the progression toward the intersection space IS_{S1/S0} (refs. 11,32) represented by a conical intersection (crossing) point. The dihedral angle between the bisectors a and a' (τ) represents the orbital overlap. **d**, The relationship between C11=C12 twisting (expressed in terms of α and represented by the motion of C10 and C13) and HC11=C12H out-of-plane wagging (expressed in terms of δ_{op} and represented by the motion of H11 and H12) at the S₁-to-S₀ decay point determines whether the trajectory is successful (the overlap between lobes a and b' increases to form a *trans* π -bond) or unsuccessful (the overlap between lobes a and a' increases to form a *cis* π -bond). **e**, Hypothetical S₁ PES-induced in-phase nuclear dynamics along the reaction coordinate leading to a maximum $\Phi_{cis-trans}$ (largest fraction of successful decays). The population, initially represented by a Boltzmann distribution, propagates along α (top) and δ_{op} (bottom) with a phase relationship leading to decay at points dominated by δ_{op} (dt> 0 (refs. δ_{op}).

forces generated by the steep S_1 PES synchronize the trajectories that initially describe a compact 'in-phase" progression. However, such a progression starts to break down just 15 fs after photoexcitation through a fractional but still organized process. The analysis of this process in terms of coupled nuclear and electronic changes discloses a theoretical framework that appears instrumental for the comprehension and control of the observed $\Phi_{cis-trans}$ value.

This article is organized as follows. First, we describe the results of Rh dynamics simulations showing that (1) population desynchronization/splitting occurs along the α mode due to a mixing of the S_1 and S_2 electronic states, (2) the $\Phi_{cis-trans}$ value is the result of

contributions associated with each generated subpopulation and (3) the splitting is modulated by the opsin electrostatics. Based on these findings, we propose a mechanistic framework for the modulation of $\Phi_{\text{cis-trans}}$ in opsin-based receptors. Finally, the same results were employed to hypothesize a possible trade-off between photochemical and thermal isomerizations, which may have shaped the $\Phi_{\text{cis-trans}}$ value observed for Rh.

Results

 S_1 **population splitting.** The validation of the constructed Rh model and the stability of the population dynamics simulation

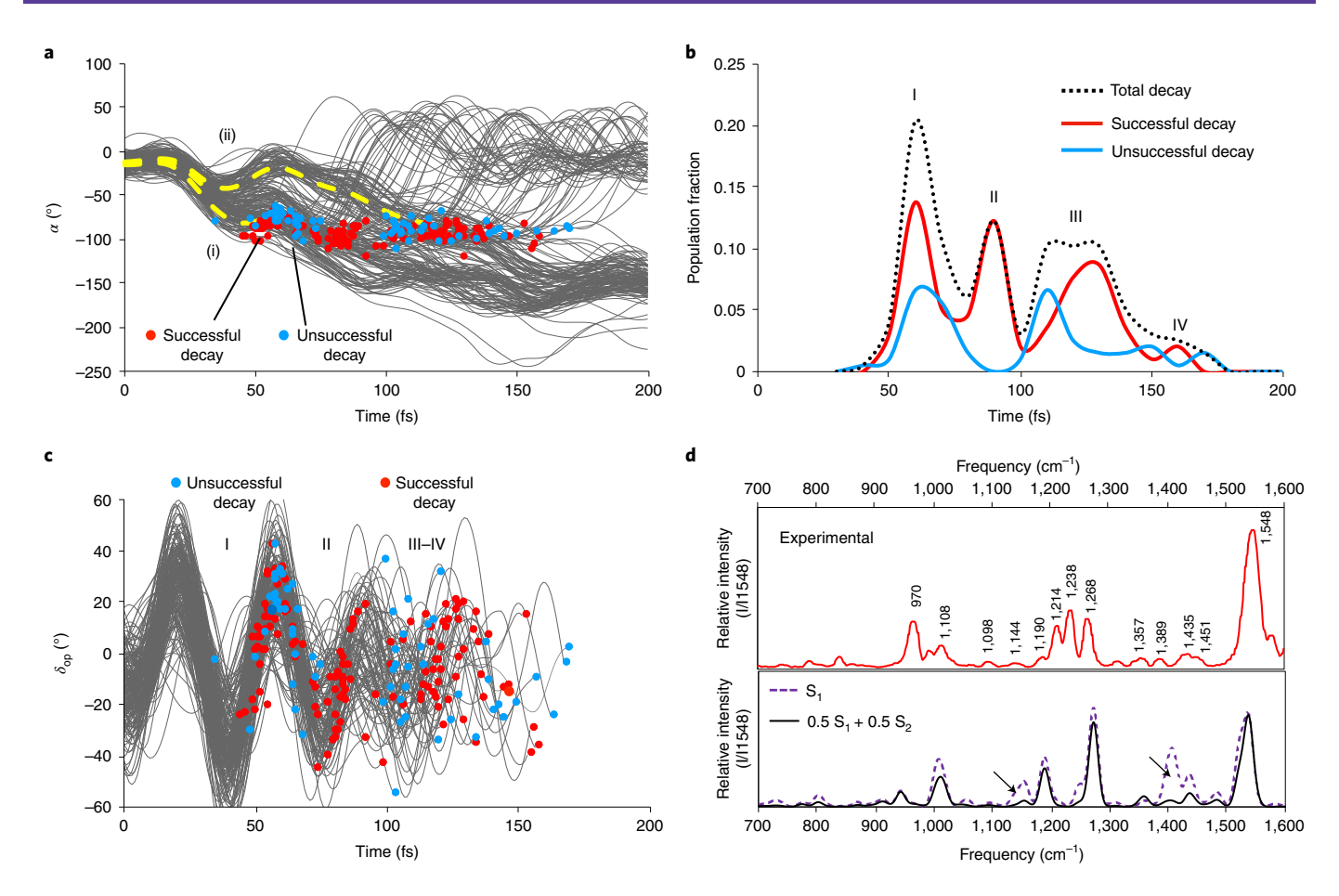


Fig. 2 | Rh population dynamics. a, Time progression of α along a set of 200 trajectories simulating the S₁ population at room temperature and showing a motion initially coherent over the statistical ensemble³⁴. The circles represent decay from S₁ to S₀. The yellow splitting dashed curves serve as guides tracing fast (i) and slow (ii) decaying subpopulations. **b,** Oscillatory character of the simulated S₁ population decay for both successful and unsuccessful trajectories. The total decay is also shown. The four peaks have been resolved on the assumption that the standard deviation of the average decay time of the peaks has to be <10 ±1fs. **c,** Time progression of δ_{op} along the same trajectories. **d,** Effect of the involvement of the S₂ state on the simulated resonance Raman spectrum of Rh: experimental spectrum³⁵ (top) and comparison of the resonance Raman spectra simulated using the S₁ gradient and an equal mixture of S₁ and S₂ gradients according to the weighted-gradients method³⁶ (bottom). The arrows point to regions requiring both states for a correct description. The relative intensity (I/I1548) is plotted with respect to the most intense mode at 1548 cm⁻¹ (see Supplementary Section 10).

are documented in Supplementary Sections 1–3. In Fig. 2a we show the evolution of α for the entire set of trajectories. It is apparent from an inspection of the figure that S_1 -to- S_0 decay occurs when α has a value of $-90\pm30^\circ$ (that is, when the π -bond of C11=C12 is broken) and lasts for ~150 fs, starting with an early decay event at ~35 fs . The trajectories can be used to compute a number of observables, including the S_1 lifetime, photoproduct appearance time and $\Phi_{cis-trans}$. Supplementary Table 1 shows that the computed values are consistent with experimental observations, including the relevant S_1 vibrational frequencies and the isotopic modulation of $\Phi_{cis-trans}$ (ref. 13). Furthermore, the simulation complies with the relationship linking the sign of $d\delta_{op}/dt$ with successful isomerizations (Supplementary Fig. 4a), as 73% of the successful trajectories have, at decay, $d\delta_{op}/dt > 0$.

As discussed above (Fig. 1e), to achieve a maximum quantum efficiency, Rh would generate a S_1 population that decays when $d\delta_{op}/dt > 0$. However, the data in Fig. 2a show that, along α , the population remains compact for less than 30 fs and then splits. The splitting produces subpopulations decaying at different times, forming peaks I–IV (Fig. 2b), which feature, as expected, increasing δ_{op} values for groups of successful decay events (Fig. 2c). Peak I corresponds to the fastest decaying subpopulation, which decays between 35 and 80 fs (curve (i) in Fig. 2a). In contrast, for the slowest decaying

subpopulation, the initial counterclockwise rotation changes to a clockwise rotation, pushing α back towards 0° (curve (ii) in Fig. 2a), and then reverts to decay at times ranging from 110 to 170 fs, forming peaks III and IV. The occurrence of splitting does not appear to depend on the specific QM/MM model employed or on the type of visual pigment, although peak height and distribution may differ substantially. Such behaviour is supported in Supplementary Fig. 5, which displays data from different QM/MM models.

The results above indicate that $\Phi_{cis-trans}$ is the sum of fractional contributions from different subpopulations. Because each subpopulation hits $\mathrm{IS}_{\mathrm{S1/S0}}$ at a different time and δ_{op} phase, it would display a different $\mathrm{d}\delta_{\mathrm{op}}/\mathrm{d}t$ distribution, yielding a different $\Phi_{cis-rans}$ contribution. It is thus apparent that the splitting mechanism, which would determine the number of subpopulations and their dynamics, is critical. More specifically, it is apparent that the nuclear forces causing the splitting, as well as their relation to the S_1 electronic structure, have to be investigated.

The ultrashort timescale of the splitting event suggests that Franck–Condon (FC) forces are its primary cause. Such forces are experimentally fingerprinted by the Rh resonance Raman (RR) spectrum displayed in Fig. 2d (top). The simulation of this spectrum may help to formulate a correct mechanistic hypothesis for the splitting. We found that, when only S_1 forces computed for the

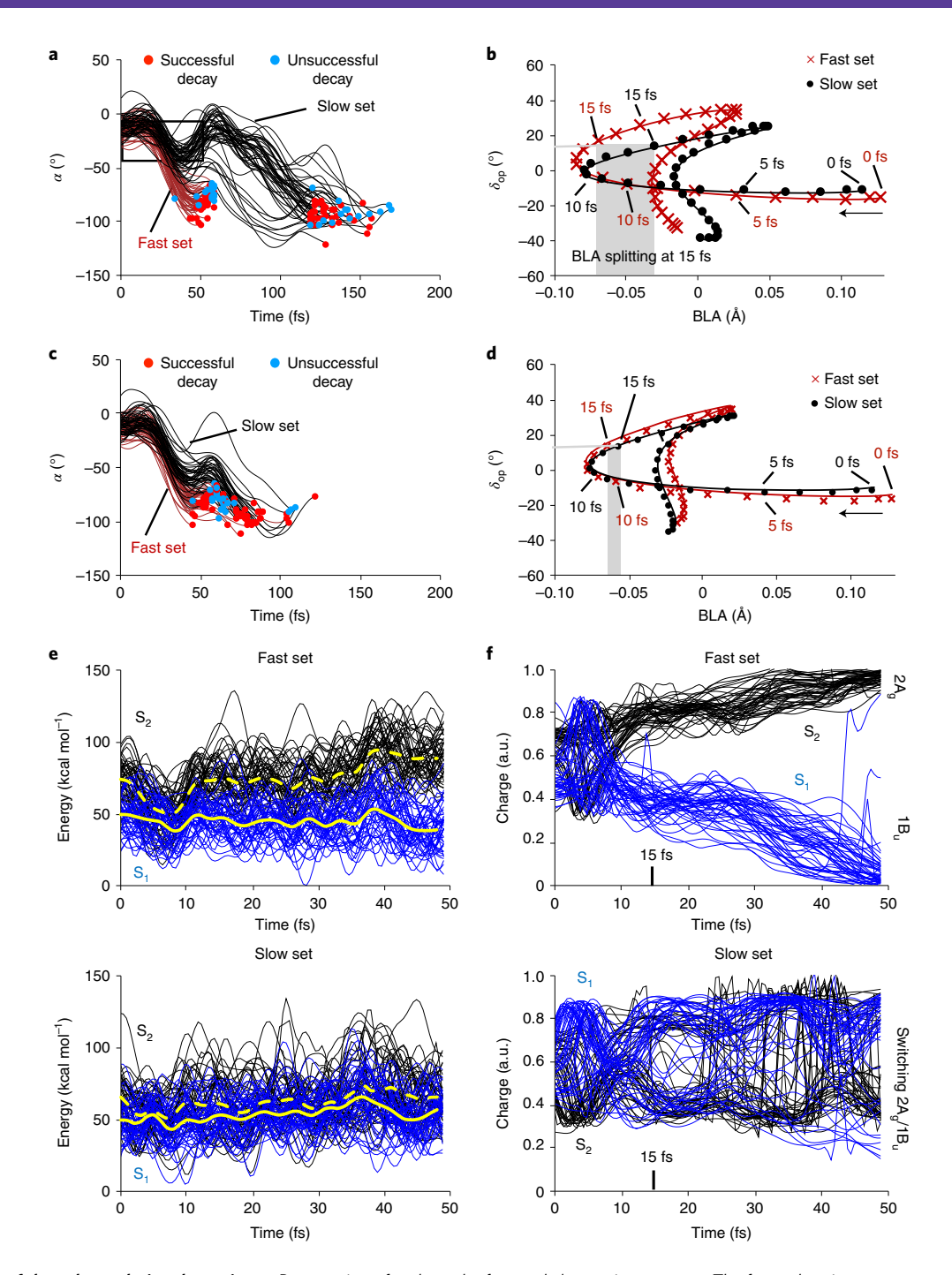


Fig. 3 | **Analysis of the subpopulation dynamics. a**, Progression of α along the fast and slow trajectory sets. The framed region represents the investigated α (-10 to -40°) and time (0-50 fs) window. **b**, Progression along the average BLA and δ_{op} values for the fast and slow sets. **c**, Progression of α along the fast and slow trajectory sets for a Rh model with opsin atomic charges set to half of their original values. d, Progression along the average BLA and δ_{op} values for the fast and slow sets for the half-charge Rh model. **e**, Time evolution of the S₁ and S₂ potential energy profiles for the fast (top) and slow (bottom) trajectory sets. **f**, Time evolution of the S₁ and S₂ charge transfer magnitude for the fast (top) and slow (bottom) sets. The 1B_u and 2A_g labels refer to the symmetry of the electronic wavefunction of a reference planar all-trans polyene.

equilibrium Rh structure were employed to simulate the spectrum (Fig. 2d, bottom), certain observed spectral regions were poorly reproduced, suggesting the involvement of other electronic states in the population dynamics. Indeed, as is also shown in Fig. 2d (bottom), the RR spectrum simulated using an effective gradient with an equal weight of the S_2 gradient with respect to the S_1 gradient displayed a substantial improvement (Supplementary Section 10). Accordingly, we hypothesized that a mixing of the S_1

and S_2 electronic characters during the initial S_1 dynamics is implicated in the population splitting.

 S_2 and S_1 mixing and splitting mechanism. The mixing of the S_1 and S_2 electronic characters was investigated by focusing on two sets of trajectories. As shown in Fig. 3a, the first (49 trajectories) and second (48 trajectories) set represent the fastest and slowest subpopulations, respectively. At time zero, the two sets

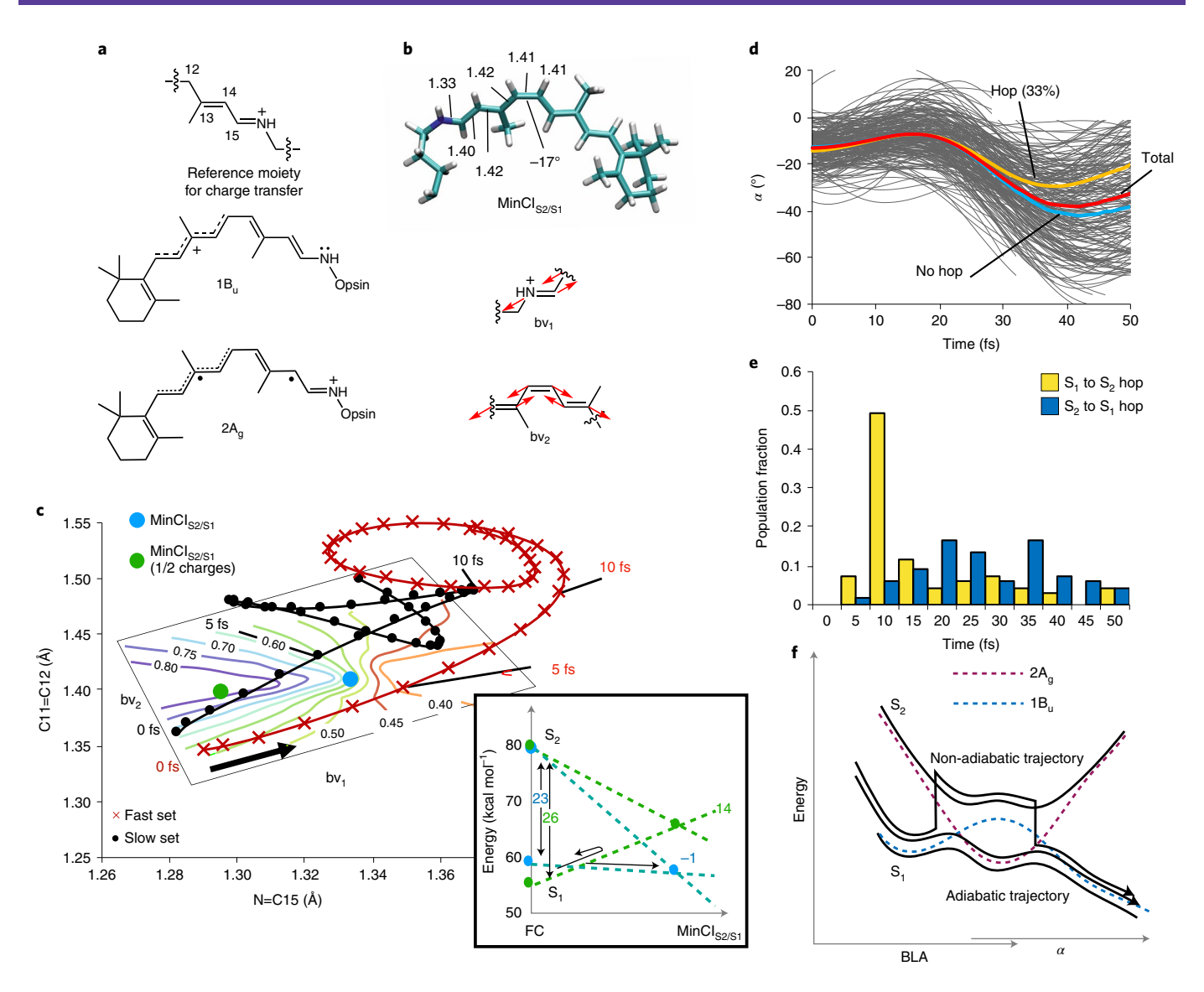


Fig. 4 | Analysis of excited-state mixing. a, Structures of the rPSB11 reference moiety used to estimate the charge transfer (moiety for total charge), and the Lewis structures representing the $1B_u$ and $2A_g$ electronic characters of rPSB11. **b**, Structure of MinCl_{52/S1} and pictorial representations of the branching plane vectors bv_1 and bv_2 . **c**, Progression along the average N=C15 and C11=C12 components of BLA for the fast and slow sets. The contour diagram represents the change in charge transfer plotted along the branching plane. The inset in the bottom right shows the effect of the charge reduction on the S_1 energy differences between the MinCl_{52/S1} and FC regions. With half charges, the MinCl_{52/S1} is destabilized (from -1 to 14 kcal mol⁻¹) relative to FC. **d**, Initial progression of α along 200 trajectories released along the S_1 PES and allowed to hop to the S_2 PES. The average progression of total 200 trajectories is indicated by the red curve. The average progression of the subset undergoing at least one non-adiabatic transition (33 and 14% of the total number of trajectories when using S_1 and S_2 or S_0 , S_1 and S_2 state averaging, respectively; see the Methods section and Supplementary Section 16) or no transition are shown by the yellow and blue curves, respectively. **e**, Time distribution of the S_1 -to- S_2 and S_2 -to- S_1 hops. **f**, Schematic representation of an adiabatic and non-adiabatic (that is, hopping) trajectory in the vicinity of MinCl_{52/S1}. The dashed curves represent, pictorially, the 'diabatic' energy associated with the $1B_u$ and $2A_g$ electronic characters. The magnitude of the corresponding S_2/S_1 NADC modulus along a three-dimensional cut of the S_1 -PES is given in Extended Data Fig. 1.

are indistinguishable in terms of the α , $\delta_{\rm op}$ and BLA distributions, indicating a weak dependence of the population splitting on the initial conditions (Supplementary Fig. 6). However, the progression along BLA and $\delta_{\rm op}$ reported in Fig. 3b shows that the two sets start to split along BLA after just 15 fs. We could also demonstrate that the splitting is modulated by the electrostatics of opsin. Indeed, Fig. 3c,d shows that the splitting is reduced when the simulation is repeated after setting all opsin atomic charges to half of their original values (Supplementary Fig. 8) and, therefore, effectively decreasing the electrostatic field acting on the chromophore. After calculating the full set of 200 trajectories with the

half-charge model, we confirmed that the S_1 population remains more compact and decays to S_0 on a faster timescale. The fact that such behaviour is closer to a single population decay (Fig. 1e) led us to recompute $\Phi_{cis-trans}$, which was found to be 0.72 and therefore higher than the 0.68 value obtained for the unaltered Rh model. This suggests that (1) the splitting decreases the $\Phi_{cis-trans}$ value and (2) the value is not maximized in Rh.

The hypothesis that the mixing of the S_1 and S_2 electronic characters during the initial S_1 relaxation leads to a slower α progression was initially investigated by computing the evolution of the S_2 – S_1 gap and S_1 electronic character along the fast and slow trajectory sets.

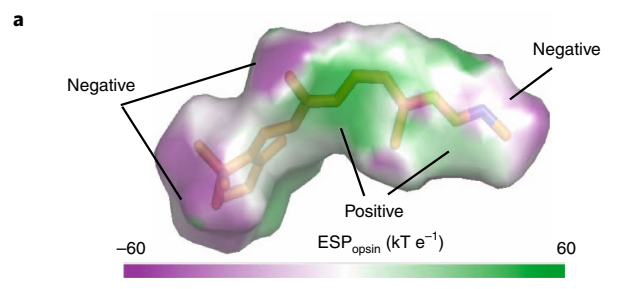
Figure 3e shows that both the fast (top) and slow (bottom) sets enter a region where S_2 and S_1 become degenerate (that is, the $IS_{S2/S1}$ region) in ~10 fs. However, although this region is abandoned in the former case, the slow set dwells in the degeneracy region for over 50 fs (see also Supplementary Fig. 9). These differences are reflected in the corresponding variations in the charge distribution in the chromophore and, therefore, the electronic character. Although the fast trajectories (Fig. 3f, top) experience a gradual change in their charge distributions (for instance, the charge of the N-containing backbone moiety, Fig. 4a, top), the trajectories of the slow set (Fig. 3f, bottom) show multiple sudden variations in charge, pointing to multiple changes of the S_1 electronic character, consistently with transits close to $IS_{S2/S1}$.

Motion in the region of a S_2/S_1 conical intersection. The results shown in Fig. 3e,f can be interpreted by recalling that at time zero, the S_1 and S_2 states of Rh are dominated by $1B_u$ and $2A_g$ electronic character, respectively¹². As illustrated in Fig. 4a (middle), the $1B_u$ character is described by a charge transfer (ionic) configuration in which the C11=C12 bond acquires single-bond character, prompting torsional deformation and reactivity. On the other hand, the $2A_g$ character is dominated by a double excitation and has diradical character (Fig. 4a, bottom), featuring a C11=C12 bond with residual double-bond order. Accordingly, the slow set would be associated with $1B_u/2A_g$ character mixing and inversion restraining double-bond twisting. Remarkably, such an inversion is not seen along the trajectory sets computed using the Rh model with half opsin charges, indicating that the change in opsin electrostatics drives the two trajectory sets away from the $1S_{S2/S1}$ region.

The points belonging to the $IS_{52/S1}$ region are represented by the S_2/S_1 minimum energy conical intersection (MinCI_{52/S1}) structure (Fig. 4b), which is located below the FC point. From inspection of the MinCI_{52/S1} branching plane cross-section shown in Fig. 4c, it is clear that the fast and slow trajectory sets travel on opposite sides of MinCI_{52/S1}. Although the fast set propagates along the side dominated by $1B_u$ character, the slow set enters the opposite side, featuring a region with greater $2A_g$ character, and then re-enters a region with $1B_u$ character. The slow set should therefore transit in a more bounded region where its progression is restrained. Remarkably, both fast and slow trajectory sets propagate on the same side of MinCI_{52/S1} when the opsin charges are halved (Supplementary Fig. 10). In fact, the scaling of the opsin electrostatics leads to the displacement of MinCI_{52/S1} to a higher energy location (see inset in Fig. 4c) that is avoided by the majority of the trajectories.

The above conclusions are supported by Mayer's analysis of the S_2 and S_1 wavefunctions (Supplementary Fig. 17), which show distinct free valences for the fast set (that is, at the putative radical centres C9 and C14 the free valences are around 0.5 and 0.2 for S_2 ($2A_g$) and for S_1 ($1B_u$), respectively), but not for the slow set (for example, around 0.3 at both C9 and C14 for both S_2 and S_1), indicating character mixing.

The presence of $1B_u/2A_g$ mixing in the slow trajectory set indicates not only increased bonding along the S1 PES, but also the possibility of non-adiabatic transitions. This hypothesis has been investigated by recomputing the dynamics of the initial 50 fs over the entire population at a level of theory that explicitly incorporates the S₂ PES (see Methods section). As reported in Fig. 4d-f, when this PES is included in the calculation, hops from S_1 to S_2 are detected along the trajectories, suggesting that non-adiabatic effects may contribute to restrain the motion of the slow set with respect to the fast set (Supplementary Sections 14–16). Indeed, Fig. 4d shows that the trajectories associated with a slower α progression display a higher percentage of sequential $S_1 \rightarrow S_2$ and $S_2 \rightarrow S_1$ transitions. This result is in line with the hypothesis that larger non-adiabatic coupling (NADC) characterizes the slow α motion. This was confirmed by mapping the NADC modulus along S₁ PES cross-sections spanned by the critical modes α , δ_{op} and BLA. The results displayed



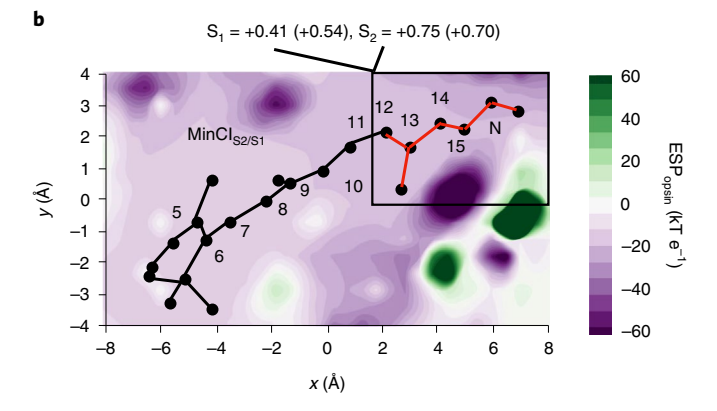


Fig. 5 | Opsin electrostatic potential at MinCl_{s2/S1}, **a**, ESP_{opsin} map of the solvent-accessible surface (solvent radius 1.4 Å) of the Rh chromophore. **b**, ESP_{opsin} cross-section along the conjugated framework. The fraction of S₁ and S₂ charges on the chromophore's Schiff base region (framed moiety in red) are given in a.u. = e above the image. The corresponding FC values are given in parentheses.

in Extended Data Fig. 1 show that, although at the initial α values (that is, at the beginning of the S₁ relaxation) there is no remarkable difference between slow and fast populations, at $\alpha = -20^{\circ}$ the slow set moves closer to the region with high NADC modulus.

Although the results above would point to a non-adiabatic or mixed adiabatic/non-adiabatic origin of the S₁ population splitting, a comparative analysis of the initial population dynamics computed without and with the S₂ PES points to a very limited difference in geometrical progression and timescale and, therefore, population splitting. This points to a dominant role played by the topography of the adiabatic S₁ PES (that is, its slopes, barriers and paths), which appears not to be qualitatively altered by the employed level of theory. In other words, although it is possible that the splitting involves a mixed adiabatic/non-adiabatic mechanism (that is, comprising the two types of trajectories depicted in Fig. 4f), the hopping events occurring along several trajectories do not qualitatively change the dynamics driven by the S₁ PES.

Effect of protein electrostatics. To explain how the scaled opsin charges modify the S_1 PES and, therefore, the trajectory progression and splitting, we mapped the protein electrostatic potential (ESP_{opsin}). It is apparent that, although the ESP_{opsin} has a complex structure (Fig. 5a), a suitable cross-section (Fig. 5b) shows that it is more negative in the Schiff base region rather than in the β-ionone region. It is thus possible to hypothesize that the ESP_{opsin} better stabilizes the $2A_g$ character than the $1B_u$ character, leading to a decrease in the S_2 - S_1 energy gap (Supplementary Fig. 15). In fact, the charges of S_2 and S_1 in the Schiff base region of the chromophore (Fig. 5b) show a greater charge for the S_2 state, indicating $2A_g$ character. The ESP_{opsin} decrease would thus lead to a destabilization of S_2 and displacement of MinCI_{S2/S1} to higher energy (from -1 to +14 kcal mol⁻¹ with respect to FC), far from the S_1 relaxation path (compare the blue and green circles in Fig. 4c).

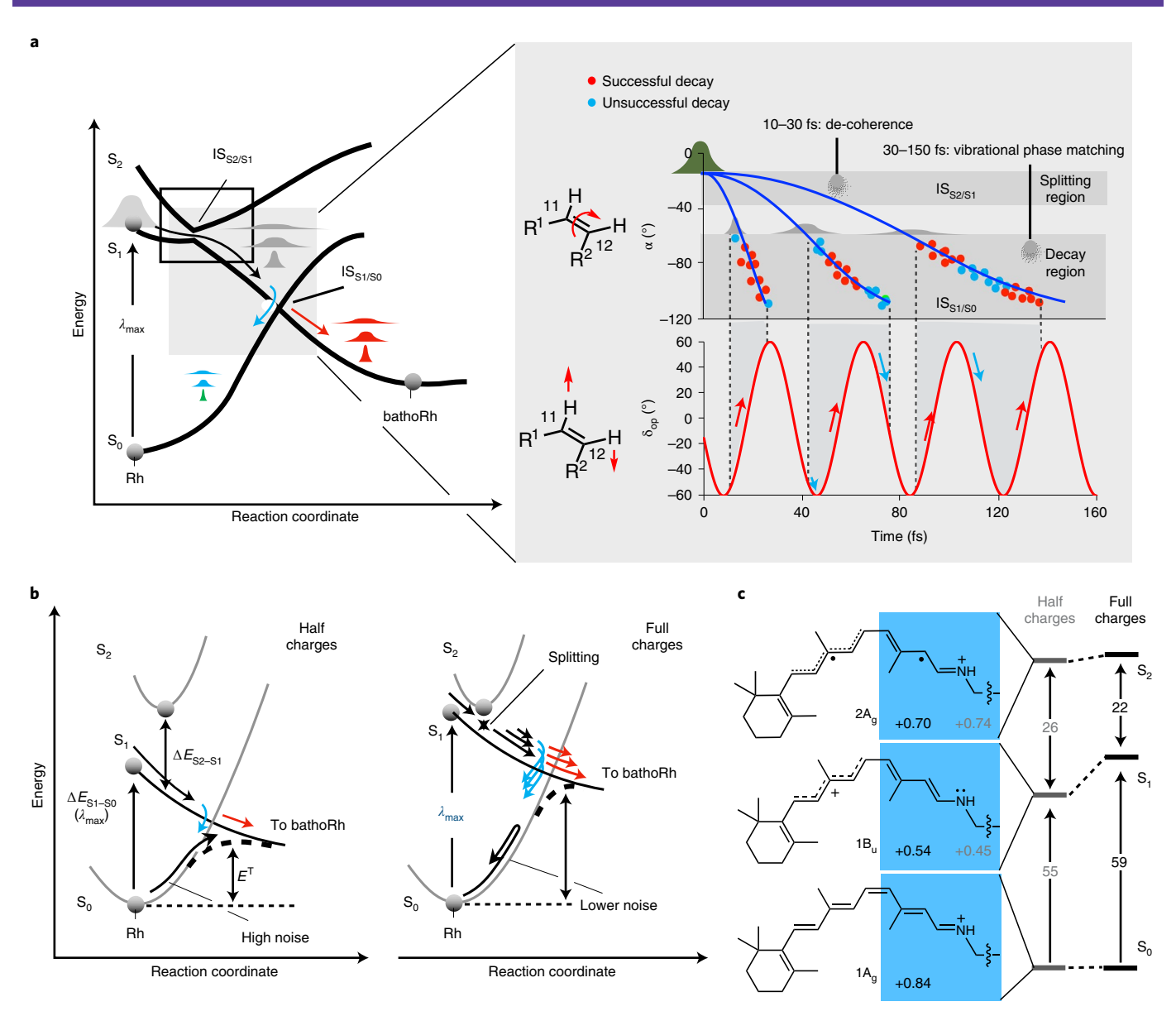


Fig. 6 | The mechanism controlling $\boldsymbol{\Phi}_{cis-trans}$ **and its possible origin. a**, Three electronic states and two intersection spaces, IS_{52/S1} and IS_{52/S1} are involved in the primary event in vision. IS_{52/S1}, which is accessed by relaxing along the lower intersecting state, mediates population splitting, whereas IS_{51/S0} is accessed from the higher intersecting state and mediates the rPSB11 branching occurring at decay (left). The relationship between decay time and the phase of the hydrogen out-of-plane wagging determines the $\boldsymbol{\Phi}_{cis-trans}$ contribution of each subpopulation (right). **b**, Trade-off between thermal noise (λ_{max}) and population splitting. **c**, Inverse proportionality between the FC computed S₁ and S₂ charges on the chromophore's Schiff base region (framed moiety) and S₀-S₁ and S₂-S₁ energy gap (in kcal/mol) changes upon decreasing the protein charges.

Supplementary Figs. 15–17 demonstrate that the described effects of ESP_{opsin} are independent of the employed levels of theory, including multistate multiconfiguration levels (XMS-CASPT2 and XMCQDPT2, ref. 19) and expanded basis set (ANO-L-VDZP). To further support our interpretation, XMS-CASPT2/ANO-L-VDZP numerical gradients were employed to locate the S $_2$ energy minimum (MinS $_2$) in a simplified Rh model. The calculation indicates that MinS $_2$ is located 2 kcal mol $^{-1}$ below the FC point (Supplementary Fig. 18), and that it is not far from being degenerate (that is, a S $_2$ –S $_1$ gap of 10 kcal mol $^{-1}$).

Discussion and conclusions

The results above connect an opsin-induced S_1 population splitting to the $\Phi_{cis-trans}$ value of a dim-light visual pigment. This connection is based on two findings. The first is that $\Phi_{cis-trans}$ is the sum of

contributions associated with different subpopulations, and the second is that the splitting generating the subpopulations is governed by the opsin electrostatics. We now discuss the Rh photoisomerization mechanism on the basis of a theoretical framework incorporating these results.

As outlined in Fig. 6a, immediately after vertical $S_0 \rightarrow S_1$ excitation, the Rh population starts a phased motion along the S_1 reaction coordinate. However, the population enters a region with a reduced $S_2 - S_1$ gap where a set of subpopulations form in 15 fs. Each subpopulation then propagates with a different timescale and δ_{op} phase. Thus, the observed $\Phi_{cis-trans}$ value must be the consequence of the synchronization between population splitting at $IS_{S2/S1}$ and the generation of favourable $d\delta_{op}/dt$ versus $d\alpha/dt$ phases at $IS_{S1/S0}$. This suggests that $\Phi_{cis-trans}$ should be studied, as mentioned by Warshel et al.²⁰, using simulations accounting for multiple modes

and states. In fact, the described mechanism appears to be closely related to the one reported by Lim and $\rm Kim^{21}$, who proposed that the behaviour of molecules reaching the reactive intersection space (in our case $\rm IS_{S1/S0}$) is determined by early events (that is, a sort of memory effect).

According to our calculations, the involvement of S_2 , with its $2A_g$ character, in the Rh dynamics is limited to the initial relaxation. However, the temporary $2A_g$ character not only justifies the population splitting, but also its sensitivity to the opsin electrostatic field and, therefore, amino acid sequence. In other words, a variation in the sequence, such as one caused by natural selection, may transform a single population (Fig. 1e) into multiple subpopulations (Fig. 6a) and modify the resulting $\Phi_{cis-trans}$ value. Note that, due to the complexity of this process, the details of the QM/MM model alter the number and distribution of the simulated subpopulations, but not the fact that they are generated nor their sensitivity to the opsin electrostatics.

It remains to be seen whether the mechanism presented above has a significance for the adaptation of a visual pigment to dim-light conditions. Such a pigment would need maximum light sensitivity and, therefore, the conclusion that population splitting makes the optimization of $\Phi_{cis-trans}$ complex or, as suggested by our results, decreases its value is counterinuitive. However, the light sensitivity of Rh depends on both $\Phi_{cis-trans}$ and the noise associated with rPSB11 thermal isomerization. As we will now explain, it is possible to argue that population splitting is the byproduct of a trade-off between photochemical and thermal isomerizations leading to a maximum light sensitivity.

A trade-off hypothesis can be formulated starting from the reported⁵ inverse proportionality between λ_{\max} and E^{T} (compare the left and right parts of Fig. 6b), where E^{T} is the energy barrier controlling the thermal (S₀) isomerization of rPSB11. This inverse proportionality implies that Rh may have evolved to absorb blue light to maximize E^{T} and, in turn, decrease the rate of thermal Rh activation. However, a shorter λ_{\max} is achieved by selecting an opsin sequence whose electrostatics destabilize S_1 with respect to S_0 . Because S_0 and S₂ have similar charge distributions (Fig. 6c), such destabilization must lead to a smaller S2-S1 gap and, as a consequence, population splitting. This is in line with the documented effects of ${\rm ESP}_{\rm opsin}$ scaling causing, simultaneously, a decrease in ΔE_{S1-S0} (that is, a redshift in λ_{max}) and an increase in $\Delta E_{\text{S2-S1}}$. The small S_2 – S_1 gap found in Rh would thus be the result of sequence variations designed to decrease its thermal noise but that also induce a counterproductive $\Phi_{cis-trans}$ decrease due to population splitting. Such a hypothesis remains to be experimentally assessed.

In conclusion, the documented connection between population splitting and $\Phi_{cis-trans}$ advances the construction of the theoretical framework necessary for understanding Rh light sensitivity and reveals a novel effect of the opsin electrostatics on the primary event in vision^{22–25}. Such a connection is not likely to be a common feature across the vast rhodopsin family, even if evidence exists for its involvement in microbial rhodopsins²⁶. On the other hand, the presented isomerization efficiency theory not only goes beyond the seminal one-dimensional Landau-Zener model²⁷ holding that a high speed along lpha determines a high $arPhi_{cis-trans}$, but also provides a distinct and multimodal scenario for the involvement of the S₂ state with respect to past hypotheses²⁸. At the same time, it raises important questions about our ability to quantitatively predict the effect of mutations on $\Phi_{cis-trans}$, as this would require a comprehension of the coupled electron-nuclear dynamics^{29,30} and possible geometric phase effects³¹ occurring very early during the dynamics of biological chromophores.

Online content

Any methods, additional references, Nature Research reporting summaries, source data, extended data, supplementary information, acknowledgements, peer review information; details of

author contributions and competing interests; and statements of data and code availability are available at https://doi.org/10.1038/s41557-022-00892-6.

Received: 28 May 2020; Accepted: 12 January 2022;

Published online: 03 March 2022

References

- Ernst, O. P. et al. Microbial and animal rhodopsins: structures, functions, and molecular mechanisms. Chem. Rev. 114, 126–163 (2014).
- Khorana, H. G. Rhodopsin, photoreceptor of the rod cell. An emerging pattern for structure and function. J. Biol. Chem. 267, 1–4 (1992).
- Peteanu, L. A., Schoenlein, R. W., Wang, Q., Mathies, R. A. & Shank, C. V. The first step in vision occurs in femtoseconds: complete blue and red spectral studies. *Proc. Natl Acad. Sci. USA* 90, 11762–11766 (1993).
- Polli, D. et al. Conical intersection dynamics of the primary photoisomerization event in vision. *Nature* 467, 440–443 (2010).
- Gozem, S., Schapiro, I., Ferre, N. & Olivucci, M. The molecular mechanism of thermal noise in rod photoreceptors. *Science* 337, 1225–1228 (2012).
- Dartnall, H. J. A. The photosensitivities of visual pigments in the presence of hydroxylamine. Vision Res. 8, 339–358 (1968).
- Wang, Q., Schoenlein, R., Peteanu, L., Mathies, R. & Shank, C. Vibrationally coherent photochemistry in the femtosecond primary event of vision. *Science* 266, 422–424 (1994).
- Kukura, P. Structural observation of the primary isomerization in vision with femtosecond-stimulated Raman. Science 310, 1006–1009 (2005).
- Johnson, P. J. M. et al. Local vibrational coherences drive the primary photochemistry of vision. *Nat. Chem.* 7, 980–986 (2015).
- 10. Mathies, R. A. A coherent picture of vision. *Nat. Chem.* 7, 945–947 (2015)
- Schapiro, I. et al. The ultrafast photoisomerizations of rhodopsin and bathorhodopsin are modulated by bond length alternation and HOOP driven electronic effects. *I. Am. Chem. Soc.* 133, 3354–3364 (2011).
- Gozem, S., Luk, H. L., Schapiro, I. & Olivucci, M. Theory and simulation of the ultrafast double-bond isomerization of biological chromophores. *Chem. Rev.* 117, 13502–13565 (2017).
- 13. Schnedermann, C. et al. Evidence for a vibrational phase-dependent isotope effect on the photochemistry of vision. *Nat. Chem.* **10**, 449–455 (2018).
- Weingart, O. et al. Product formation in rhodopsin by fast hydrogen motions. Phys. Chem. Chem. Phys. 13, 3645–3648 (2011).
- Sen, S. & Schapiro, I. A comprehensive benchmark of the XMS-CASPT2 method for the photochemistry of a retinal chromophore model. *Mol. Phys.* 116, 2571–2582 (2018).
- Gozem, S. et al. Mapping the excited state potential energy surface of a retinal chromophore model with multireference and equation-of-motion coupled-cluster methods. J. Chem. Theory Comput. 9, 4495–4506 (2013).
- Andersson, K., Malmqvist, P. A., Roos, B. O., Sadlej, A. J. & Wolinski, K. Second-order perturbation theory with a CASSCF reference function. J. Phys. Chem. 94, 5483–5488 (1990).
- Luk, H. L., Melaccio, F., Rinaldi, S., Gozem, S. & Olivucci, M. Molecular bases for the selection of the chromophore of animal rhodopsins. *Proc. Natl Acad.* Sci. USA 112. 15297–15302 (2015).
- 19. Granovsky, A. A. Firefly, v.8.0.0 (Moscow State University, 2013).
- Warshel, A., Chu, Z. T. & Hwang, J. K. The dynamics of the primary event in rhodopsins revisited. *Chem. Phys.* 158, 303–314 (1991).
- Lim, J. S. & Kim, S. K. Experimental probing of conical intersection dynamics in the photodissociation of thioanisole. *Nat. Chem.* 2, 627–632 (2010).
- Warshel, A. & Chu, Z. T. Nature of the surface crossing process in bacteriorhodopsin: computer simulations of the quantum dynamics of the primary photochemical event. *J. Phys. Chem. B* 105, 9857–9871 (2001).
- Toniolo, A., Olsen, S., Manohar, L. & Martínez, T. J. Conical intersection dynamics in solution: the chromophore of green fluorescent protein. *Faraday Discuss.* 127, 149–163 (2004).
- Park, J. W. & Rhee, Y. M. Electric field keeps chromophore planar and produces high yield fluorescence in green fluorescent protein. *J. Am. Chem. Soc.* 138, 13619–13629 (2016).
- Romei, M. G., Lin, C. Y., Mathews, I. I. & Boxer, S. G. Electrostatic control of photoisomerization pathways in proteins. *Science* 367, 76–79 (2020).
- Gozem, S. et al. Excited-state vibronic dynamics of bacteriorhodopsin from two-dimensional electronic photon echo spectroscopy and multiconfigurational quantum chemistry. J. Phys. Chem. Lett. 11, 3889–3896 (2020).
- Zener, C. Non-adiabatic crossing of energy levels. Proc. R. Soc. Lond. A 137, 696–702 (1932).
- Gai, F., Hasson, K. C., McDonald, J. C. & Anfinrud, P. A. Chemical dynamics in proteins: the photoisomerization of retinal in bacteriorhodopsin. *Science* 279, 1886–1891 (1998).

- Albert, J., Hader, K. & Engel, V. Coupled electron-nuclear quantum dynamics through and around a conical intersection. J. Chem. Phys. 147, 064302 (2017).
- Olivucci, M., Tran, T., Worth, G. A. & Robb, M. A. Unlocking the double bond in protonated Schiff bases by coherent superposition of S₁ and S₂. J. Phys. Chem. Lett. 12, 5639–5643 (2021).
- Xie, C., Malbon, C. L., Guo, H. & Yarkony, D. R. Up to a sign. The insidious effects of energetically inaccessible conical intersections on unimolecular reactions. Acc. Chem. Res. https://doi.org/10.1021/acs.accounts.8b00571 (2019).
- 32. Frutos, L. M., Andruniow, T., Santoro, F., Ferre, N. & Olivucci, M. Tracking the excited-state time evolution of the visual pigment with multiconfigurational quantum chemistry. *Proc. Natl Acad. Sci. USA* **104**, 7764–7769 (2007).
- 33. Warshel, A. Bicycle-pedal model for the first step in the vision process. *Nature* **260**, 679–683 (1976).

- Miller, W. H. Perspective: quantum or classical coherence. J. Chem. Phys. 136, 210901 (2012).
- Lin, S. W. et al. Vibrational assignment of torsional normal modes of rhodopsin: probing excited-state isomerization dynamics along the reactive C₁₁=C₁₂ torsion coordinate. *J. Phys. Chem. B* 102, 2787–2806 (1998).
- Jarzęcki, A. A. & Spiro, T. G. Porphyrin distortion from resonance Raman intensities of out-of-plane modes: computation and modeling of N-methylmesoporphyrin, a ferrochelatase transition state analog. J. Phys. Chem. A 109, 421–430 (2005).

Publisher's note Springer Nature remains neutral with regard to jurisdictional claims in published maps and institutional affiliations.

© The Author(s), under exclusive licence to Springer Nature Limited 2022

Methods

Rh QM/MM model construction. The Rh QM/MM model was constructed from the 2.2 Å resolution crystallographic structure (Protein Data Bank ID: $1U19)^{37}$ and following a reported protocol 13 . The retinylidene chromophore, NH group and C_eH_2 atoms linked to the C_6 atom of the Lys296 side-chain form the QM layer. The rest of the protein forms the MM layer, described by a modified AMBER94 force field featuring specific Lys296 side-chain parameters 18,59 . A H-link atom was employed to saturate the bond between the C_e and C_6 , which is also part of the QM layer. The corresponding S_0 equilibrium geometry was obtained by QM/MM optimization at the CASSCF(12,12)/6-31G²/AMBER level. During the optimization, the QM layer, all side-chains and water molecules with at least one atom within 4 Å of any atom of the retinal chromophore were kept flexible while all remaining atoms were kept frozen. All calculations were performed with the MOLCAS/Tinker package 40,41 .

Population dynamics simulation. The QM/MM model constructed above was employed to simulate a room-temperature Boltzmann-like (that is, vibrationally incoherent) distribution described by 200 initial conditions. Briefly, a 20 ns dynamics simulation was performed using the GROMACS software 2 starting from the S_0 equilibrium geometry at the MM level of theory at 298 K, and 200 snapshots (geometries and velocities) were extracted during the dynamic simulation at intervals of 100 ps. Each snapshot was propagated at the HF/6-31G*/AMBER level for 200 fs followed by at the two-root-state-average CASSCF/6-31G*/AMBER level on the S_0 PES for 50 fs. The final geometries and velocities from the ground-state QM/MM dynamics comprised the initial conditions for subsequent S_1 population dynamics. We note that such initial conditions correspond to the effect of an ultrashort light pulse treated in the so-called 'classical' limit of an instantaneous optical transition in the Condon approximation.

We propagated 200 quantum–classical trajectories starting from the 200 initial conditions defined above for 200 fs each at the two-root-state-average CASSCF/6-31G*/AMBER level using the Tully surface-hop method and equal S_0 and S_1 weights* 3 . The trajectories yielded a simulation of the dynamics of the entire population (population dynamics). We also re-ran all 200 trajectories from the original initial conditions, but with the opsin atomic charge set to half of the original value. To study the impact of surface hopping on the initial 50 fs dynamics describing the population splitting, the full trajectory set was recomputed at both the three-root-state-average CASSCF/6-31G*/AMBER level with equal S_0 , S_1 and S_2 weights as well as with 0.0, 0.5 and 0.5 weights (equivalent to a two-root-state-average CASSCF/6-31G*/AMBER level with equal S_1 and S_2 weights).

Raman spectra simulations. Franck–Condon factors were obtained within the harmonic approximation assuming identical normal modes and vibrational frequencies in the S_0 and electronic excited states. The normal modes and vibrational frequencies of the S_0 equilibrium geometry were calculated using the QM/MM model of Rh described above and the CASSCF/6-31G*/AMBER level of theory, and S_1 and S_2 gradients were obtained using the same QM/MM model at the two-root- and three-root-state-average CASSCF wavefunction, respectively.

More details on the model construction, population dynamics simulations and Raman spectra simulations are provided in the Supplementary Information.

Data availability

The authors declare that the data supporting the findings of this study are available within the main article and the Supplementary Information. Cartesian coordinates generated along the trajectories can be found at https://doi.org/10.5281/zenodo.5826280. Source data are provided with this paper.

Code availability

The authors declare that the present research has been produced with distributed software available to the public, as also detailed in the Supplementary Information.

References

- Okada, T. et al. The retinal conformation and its environment in rhodopsin in light of a new 2.2 Å crystal structure. J. Mol. Biol. 342, 571–583 (2004).
- Cornell, W. D. et al. A second generation force field for the simulation of proteins, nucleic acids, and organic molecules. *J. Am. Chem. Soc.* 118, 2309 (1996).
- Ferré, N., Cembran, A., Garavelli, M. & Olivucci, M. Complete-active-space self-consistent-field/Amber parameterization of the Lys296-retinal-Glu113 rhodopsin chromophore-counterion system. *Theor. Chem. Acc.* 112, 335–341 (2004).
- Aquilante, F. et al. Molcas 8: new capabilities for multiconfigurational quantum chemical calculations across the periodic table. *J. Comput. Chem.* 37, 506–541 (2016).
- Ponder, J. W. & Richards, F. M. Tinker molecular modeling package. J. Comput. Chem. 8, 1016–1024 (1987).
- Pronk, S. et al. GROMACS 4.5: a high-throughput and highly parallel open source molecular simulation toolkit. *Bioinformatics* 29, 845–854 (2013).
- 43. Granucci, G. & Persico, M. Critical appraisal of the fewest switches algorithm for surface hopping. *J. Chem. Phys.* **126**, 134114 (2007).

Acknowledgements

We thank R. A. Mathies for directing our attention towards the Rh resonance Raman spectrum, B. Chang for suggesting the idea of a trade-off and S. Haacke for helpful discussions. We also thank N. Ferrè for the frequency calculation code in Molcas/Tinker and L. Barneschi for help in generating the plots in Fig. 5. The research was partially supported by the grants NSF CHE-CLP-1710191, NIH GM126627-01 and USIAS 2015, the Ohio Supercomputer Center, the Ministero dell'Istruzione, dell'Università e della Ricerca (MIUR) for a 'Dipartimento di Eccellenza 2018–2022', the Fondazione Banca d'Italia (to M.O.), the Interdisciplinary Thematic Institute QMat (as part of the ITI 2021–2028 program of the University of Strasbourg), the CNRS and Inserm via the IdEx Unistra (ANR 10 IDEX 0002), SFRI STRAT'US (ANR 20 SFRI 0012) and Labex NIE (ANR-11-LABX-0058_NIE) projects of the French Investments for the Future Program (to J.L.).

Author contributions

M.O. and X.Y. designed the study. X.Y. carried out the molecular dynamics simulations. T.A. contributed to the resonance Raman spectra simulation. X.Y., M.M., J.L. and S.G. analysed the data. M.O. and X.Y. wrote the paper. All authors discussed and commented on the manuscript.

Competing interests

The authors declare no competing financial interests.

Additional information

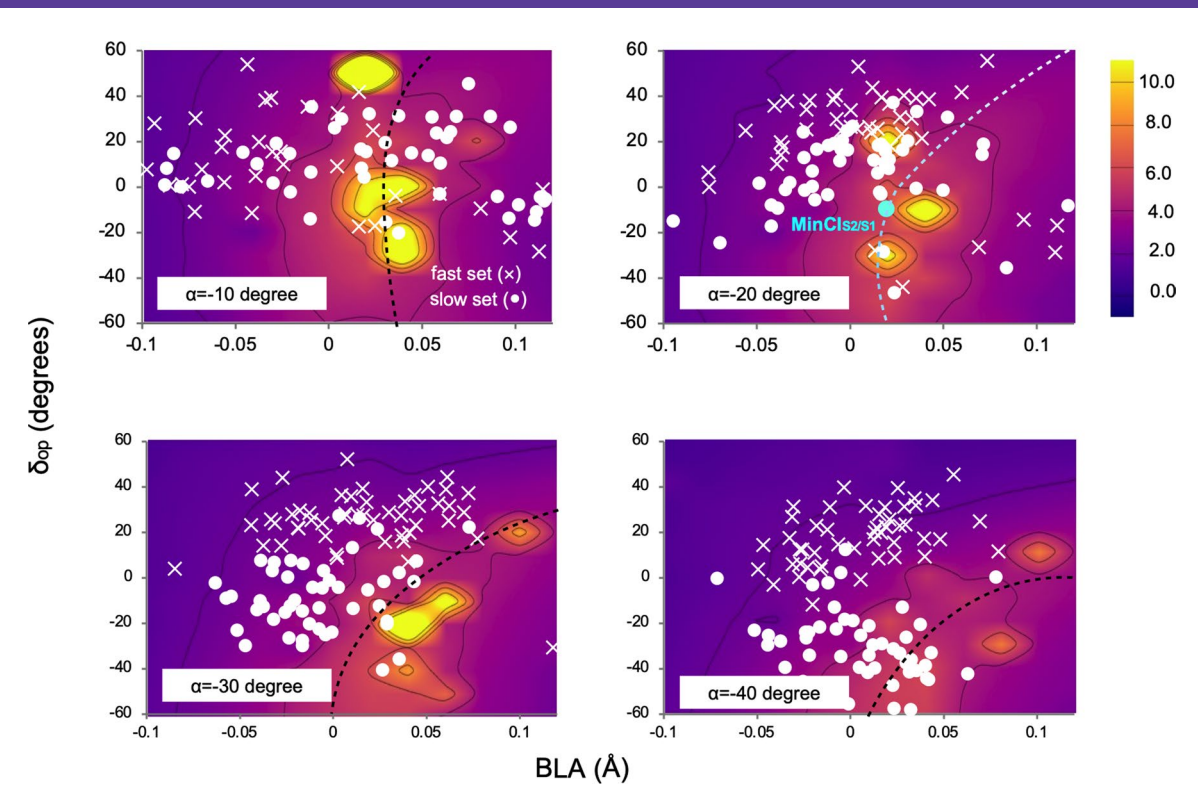
Extended data is available for this paper at https://doi.org/10.1038/s41557-022-00892-6.

 $\label{thm:continuous} \textbf{Supplementary information} \ The online version contains supplementary material available at $$https://doi.org/10.1038/s41557-022-00892-6.$

Correspondence and requests for materials should be addressed to Massimo Olivucci.

Peer review information *Nature Chemistry* thanks Todd Martinez, Young Min Rhee and the other, anonymous, reviewer(s) for their contribution to the peer review of this work.

Reprints and permissions information is available at www.nature.com/reprints.



Extended Data Fig. 1 | Non-adiabatic coupling evolution. Non-adiabatic coupling evolution. Time evolution of the magnitude of the S_2/S_1 NADC modulus (see color legend) along a 3D cut of the S_1 PES. The cut is represented by four 2D cross-sections corresponding to different α values and spanning the δ_{op} and BLA coordinates.